Energetics of M_2 Barotropic-to-Baroclinic Tidal Conversion at the Hawaiian Islands

G. S. CARTER,* M. A. MERRIFIELD,* J. M. BECKER,+ K. KATSUMATA,# M. C. GREGG,@ D. S. LUTHER,* M. D. LEVINE,& T. J. BOYD,** AND Y. L. FIRING++

*Department of Oceanography, University of Hawai'i at Manoa, Honolulu, Hawaii
+Department of Geology and Geophysics, University of Hawai'i at Manoa, Honolulu, Hawaii
#IORGC, JAMSTEC, Yokosuka, Japan
@Applied Physics Laboratory, University of Washington, Seattle, Washington
&College of Oceanic and Atmospheric Sciences, Oregon State University, Corvallis, Oregon
**Scottish Association for Marine Sciences, Oban, Argyll, Scotland
++Scripps Institution of Oceanography, La Jolla, California

(Manuscript received 15 June 2007, in final form 20 February 2008)

ABSTRACT

A high-resolution primitive equation model simulation is used to form an energy budget for the principal semidiurnal tide (M_2) over a region of the Hawaiian Ridge from Niihau to Maui. This region includes the Kaena Ridge, one of the three main internal tide generation sites along the Hawaiian Ridge and the main study site of the Hawaii Ocean Mixing Experiment. The 0.01°–horizontal resolution simulation has a high level of skill when compared to satellite and in situ sea level observations, moored ADCP currents, and notably reasonable agreement with microstructure data. Barotropic and baroclinic energy equations are derived from the model's sigma coordinate governing equations and are evaluated from the model simulation to form an energy budget. The M_2 barotropic tide loses 2.7 GW of energy over the study region. Of this, 163 MW (6%) is dissipated by bottom friction and 2.3 GW (85%) is converted into internal tides. Internal tide generation primarily occurs along the flanks of the Kaena Ridge and south of Niihau and Kauai. The majority of the baroclinic energy (1.7 GW) is radiated out of the model domain, while 0.45 GW is dissipated close to the generation regions. The modeled baroclinic dissipation within the 1000-m isobath for the Kaena Ridge agrees to within a factor of 2 with the area-weighted dissipation from 313 microstructure profiles. Topographic resolution is important, with the present 0.01° resolution model resulting in 20% more barotropic-to-baroclinic conversion compared to when the same analysis is performed on a 4-km resolution simulation. A simple extrapolation of these results to the entire Hawaiian Ridge is in qualitative agreement with recent estimates based on satellite altimetry data.

1. Introduction

Assimilation of satellite observations has shown that a significant fraction (~1/3) of barotropic (surface) tidal energy is lost in the open ocean (Egbert and Ray 2000, 2001) rather than to bottom friction in shallow marginal seas. This has led to a resurgence of interest in internal tides as a mechanism for transferring this energy into the internal wave spectrum and subsequently to dissipation. Global simulations by Simmons et al. (2004) suggest that 75% of the open ocean generation of internal tides occurs at 20 locations of rough topography, accounting for only ~10% of the area of the ocean floor.

The Hawaii Ocean Mixing Experiment (HOME; Rudnick et al. 2003; Pinkel and Rudnick 2006) investigated the conversion of barotropic-to-baroclinic tides at steep topography as well as the associated diapycnal mixing. The focus on the Hawaiian Archipelago was motivated by the dominant M_2 tide propagating perpendicular to the topography, model estimates of 15–20 GW of M_2 barotropic tidal dissipation in the region (Egbert and Ray 2001; Zaron and Egbert 2006a), and observations of low-mode, semidiurnal baroclinic tides radiating from the Hawaiian Ridge (Chiswell 1994; Dushaw et al. 1995; Ray and Mitchum 1996, 1997). Numerical model studies of barotropic-to-baroclinic tidal conversion that focused on (or encompassed) Hawaii include Kang et al. (2000), Merrifield et al. (2001), Niwa

Corresponding author address: Dr. Glenn Carter, Department of Oceanography, University of Hawai'i at Manoa, 1000 Pope Road, MSB312, Honolulu, HI 96822.
E-mail: gscarter@hawaii.edu

DOI: 10.1175/2008JPO3860.1

and Hibiya (2001), Merrifield and Holloway (2002), and Simmons et al. (2004).

One of the goals of HOME was to develop an energy budget. Rudnick et al. (2003) presented a preliminary M_2 budget for the entire Hawaiian Ridge, consisting of 20 ± 6 GW lost from the surface M_2 tide (from Egbert and Ray 2001), 10 ± 5 GW radiating outward at the 4000-m isobath as internal tides (from Merrifield and Holloway 2002), and 10 GW of local dissipation. Although this budget "approaches closure," it contains a number of possible weaknesses, including that the Egbert and Ray (2001) and Merrifield and Holloway (2002) models have different domains, that both models have coarse ($\geq$4 km) resolution, that the magnitude of barotropic-to-baroclinic conversion was not estimated, and that a more detailed analysis of the microstructure data reduced the estimate of local dissipation to 3 ± 1.5 GW (Klymak et al. 2006).

The focus of this current work is to develop an M_2 energy budget from a single simulation that partitions energy lost from the barotropic tide among barotropic and baroclinic processes. We present a 0.01° (~1 km) resolution simulation of the M_2 tide over a subregion of the Hawaiian Ridge (section 2). A subregion is used primarily because of computational constraints, although much of the ridge still has not been mapped with multibeam surveys. The model output is validated against satellite and in situ sea level measurements, velocities from two moorings, as well as microstructure observations. To calculate the energy budget, we derive barotropic and baroclinic energy equations from the model's governing equations (section 3 and the appendix). The energy budget presented in section 4 shows that of the 2.7 GW lost from the barotropic tide, 2.3 GW is converted into internal tides and the majority of that baroclinic energy radiates out of the model domain. Section 5 revisits some of the findings of Merrifield and Holloway (2002) and shows that by using 4-km resolution topography and equating conversion to baroclinic flux divergence, conversion is underestimated by ~40% when compared to the present 1-km resolution simulation. Finally, our findings are summarized in section 6.

2. Numerical simulation

a. Model setup

For this study we use the Princeton Ocean Model (POM), a three-dimensional, nonlinear, free-surface, finite-difference primitive equation model (Blumberg and Mellor 1987). For computational efficiency, the model calculates the fast-moving surface gravity waves separately from the internal structure, using a technique known as mode, or time, splitting. POM has been used for a number of previous studies of baroclinic tidal processes over idealized (e.g., Holloway and Merrifield 1999; Johnston and Merrifield 2003) and realistic (e.g., Cummins and Oey 1997; Merrifield et al. 2001; Niwa and Hibiya 2001; Merrifield and Holloway 2002; Johnston et al. 2003) topography.

POM uses the hydrostatic approximation, wherein the pressure is simply related to the weight of the water column. This is valid as long as the horizontal scales of motion are much greater than the vertical scales (Hodges et al. 2006; Mahadevan 2006). Internal tides typically meet this criterion, although exceptions include wave breaking and steepening into highly nonlinear (solitary) waves. Venayagamoorthy and Fringer (2005) found that in a bolus [a high (~2:1) aspect-ratio, self-advecting vortex core], the nonhydrostatic pressure was 37% of the total pressure. With sufficient horizontal resolution, a hydrostatic model can identify the presence of such features but cannot accurately describe them (Holloway et al. 1999; Hodges et al. 2006); lacking the dispersive (nonhydrostatic) processes, hydrostatic models tend to overestimate the steepness of the features (Hodges et al. 2006). When comparing hydrostatic and nonhydrostatic simulations, Mahadevan (2006) found it was difficult to identify the effect of the nonhydrostatic term at a horizontal resolution of 1 km.

The Mellor and Yamada (1982) level-2.5, second-moment turbulence closure scheme (MY2.5) is used by POM to calculate the vertical eddy diffusivities. This *k–l* (turbulent kinetic energy–mixing length) submodel has been used extensively for a range of applications (over 1650 citations to date, according to the Web of Science database), including the internal tide studies listed above. It should be noted that this submodel was developed for application to atmospheric and oceanic boundary layers and does not explicitly include the wave–wave interaction dynamics expected to dominate the dissipation of internal tide energy. Warner et al. (2005) found that the MY2.5 underestimated mixing in steady barotropic and estuarine flows but overestimated mixing in a wind-driven mixed layer deepening study. We find that the combination of MY2.5 and Smagorinsky horizontal diffusivity gives reasonable agreement with microstructure observations (section 4c). Finally, a quadratic bottom friction is used in POM with a logarithmic layer formulation for the coefficient (Mellor 2004).

The simulation domain extends over 20°21.8′–23°0.3′N and 160°48.3′–155°22.5′W, that is, including the main Hawaiian Islands with the exception of the

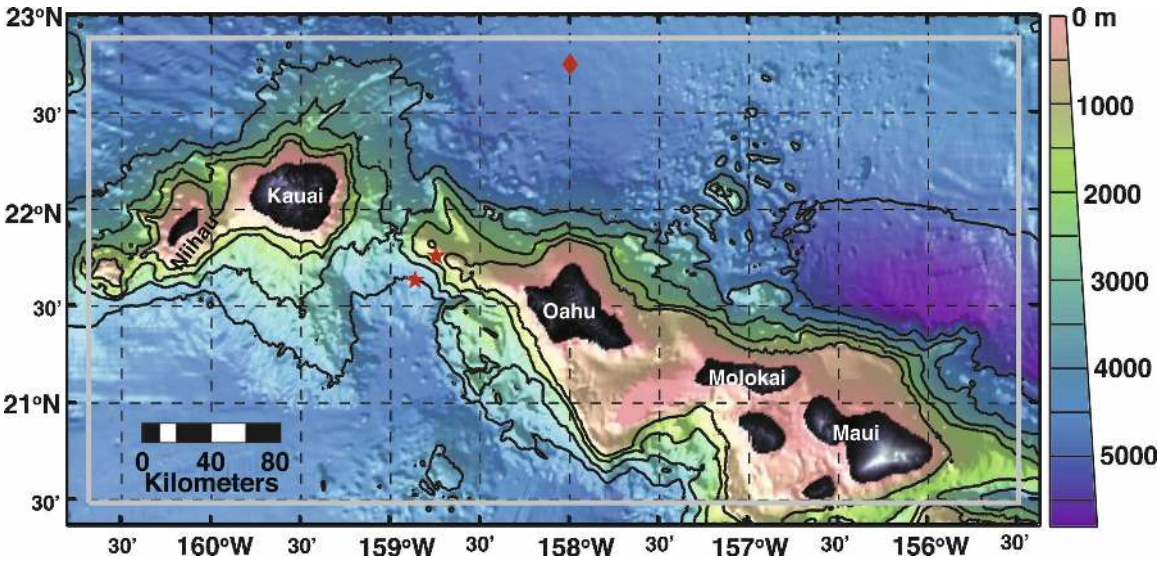

FIG. 1. Bathymetric map of the model domain, horizontal resolution is 0.01°. Contour interval is 1000 m. The gray box gives the subdomain over which the energy analysis integrations are performed. The northernmost star is the location of the A2 mooring (21°45.55′N, 158°44.75′W), and the more-southern star is the location of the C2 mooring (21°38.02′N, 158°51.80′W). The diamond marks the location of Station ALOHA (22°45′N, 158°W).

Big Island (Fig. 1). The model grid is derived from multibeam survey data and has a horizontal spacing of 0.01° (1111.9 m in latitude and 1023.5–1042.4 m in longitude), with 61 sigma levels spaced evenly in the vertical. The stratification is specified using time-averaged temperature and salinity profiles obtained over 10 yr at Station ALOHA, the Hawaii Ocean Time-series (HOT) site located 100 km north of Oahu (Fig. 1). This background stratification is horizontally uniform throughout the domain. Carter et al. (2006) and Klymak et al. (2006) found little variation outside the surface layer in stratification observed over the Hawaii Ridge. Surface buoyancy and momentum fluxes are set to zero, but the background stratification is preserved because neither horizontal nor vertical diffusivity is applied to temperature and salinity (i.e., these fields are simply advected). The model is forced at the lateral boundaries using the Flather condition (Flather 1976; Carter and Merrifield 2007), with M_2 tidal elevation and barotropic velocity from the Hawaii region TPXO6.2 inverse model (Egbert 1997; Egbert and Ray 2001; Egbert and Erofeeva 2002). Following Carter and Merrifield (2007), the baroclinic velocity fluctuations and isopycnal displacements are relaxed to zero over a 10-cell-wide region. They show that this modified relaxation scheme does not reflect energy even when a range of internal tide modes are present.

The simulations are run for 18 tidal cycles (9.3 days) from a quiescent, horizontally uniform state. Over the last six tidal cycles (3.1 days), singular value deposition (SVD) analysis is performed to obtain barotropic (depth averaged) and baroclinic (total minus depth averaged)[1] harmonic amplitudes and phases. Also, the barotropic and baroclinic energy equations [Eqs. (4) and (5) in section 3] are averaged over the same six tidal cycles.

b. Model validation

Using sea level data, Larson (1977) noted a 46° (1.5 h) M_2 phase shift across the island of Oahu, between Mokuoloe and Honolulu. Ray and Mitchum (1997) argued that most of this phase difference is likely due to the presence of the shallower topography along the Hawaiian Ridge, with additional contributions from the baroclinic tides. This is confirmed by comparing cotidal plots of our baroclinic (Fig. 2a) and the TPXO barotropic (Fig. 2b) simulations. Although most of the phase difference is in the barotropic field, the inclusion of baroclinic tides adds significant small-scale variability. The baroclinic tide has a noticeable effect on the

[1] Defining the baroclinic currents this way neglects bottom boundary layer friction. Cummins and Oey (1997) used an unstratified simulation to remove the bottom friction component from the true baroclinic tidal signal and found the results to be virtually identical to using the "total minus depth-averaged" definition. We expect this to also hold for our domain as bottom friction should be most pronounced in shallow water, and unlike Cummins and Oey (1997) there is no significant continental shelf within our domain.

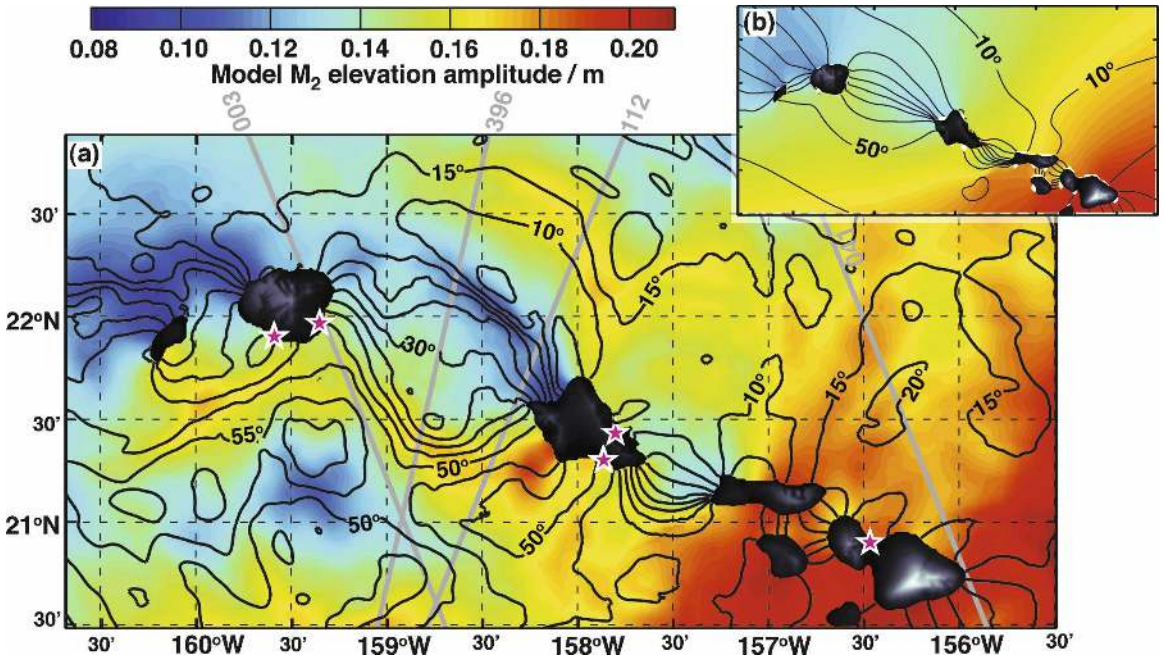

FIG. 2. The M_2 cotidal plots from (a) our baroclinic POM model run and (b) the 2D TPXO inverse model. The amplitude color range is the same in both panels. Greenwich phases are plotted with a contour interval of 5°. The five stars mark the location of long-term NOAA sea level gauges: Port Allen on the south shore of Kauai; Nawiliwili on the east shore of Kauai; Honolulu on the south shore of Oahu; Mokuoloe on the northeast shore of Oahu; and Kahului on the north shore of Maui. The gray lines mark satellite altimetry tracks. Tracks 003, 112, and 041 are TOPEX/Poseidon. Track 396 is the European Space Agency's ERS satellite.

amplitude around Oahu and Kauai. In particular, the amplitudes are reduced on the north shore of Oahu and increased on the western coast compared to the barotropic calculation.

A first check on the model skill is provided by comparing the modeled surface elevation amplitude and phase with coastal sea level observations (Table 1). National Oceanic and Atmospheric Administration's (NOAA) Center for Operational Oceanographic Products and Services (CO-OPS) maintains long-term, quality-controlled records from gauges at Port Allen, Nawiliwili, Honolulu, Mokuoloe, and Kahului (location shown with stars in Fig. 2a; the data and harmonic constants are available online at http://tidesandcurrents.noaa.gov/). Following Cummins and Oey (1997), a quantitative comparison is given using an absolute RMS error (RMSE),

$$E = \sqrt{\frac{1}{2}(A_o^2 + A_m^2) - A_o A_m \cos(G_o - G_m)}, \quad (1)$$

where subscripts o and m denote observed and modeled amplitudes (A) and phases (G). The model and observations are in good agreement, with three sites having $E < 9$ mm. The Honolulu and Mokuoloe gauges, where amplitude differences are 10–13 mm, are in Honolulu Harbor and Kaneohe Bay, respectively, which are not fully resolved by the model. The largest RMSE at Kahului is due to a 5.9° (~12 min) phase difference, which presumably is due to the narrow harbor entrance.

The baroclinic cotidal plot (Fig. 2a) shows that the surface elevation amplitudes and phases, particularly between Oahu and Kauai, are influenced by the surface bounce of the baroclinic tide. The yellow–red band is where the near-surface baroclinic displacement is in phase with the barotropic tide, resulting in increased elevation, and, conversely, the dark blue bands are out of phase. To evaluate how well we have simulated the

TABLE 1. Comparison of M_2 surface amplitudes and phases between the model and sea level gauges. The stations are part of NOAA's water-level observation network. Phase is relative to the equilibrium tide at Greenwich, E is the RMSE defined in (1).

	Model		Observed		
Station	A_m (m)	G_m (°)	A_o (m)	G_o (°)	E (m)
Port Allen	0.152	40.5	0.159	44.1	0.009
Nawiliwili	0.147	45.1	0.149	48.3	0.006
Honolulu	0.165	57.0	0.178	59.5	0.010
Mokuoloe	0.151	11.2	0.161	13.9	0.009
Kahului	0.183	14.5	0.187	8.6	0.014

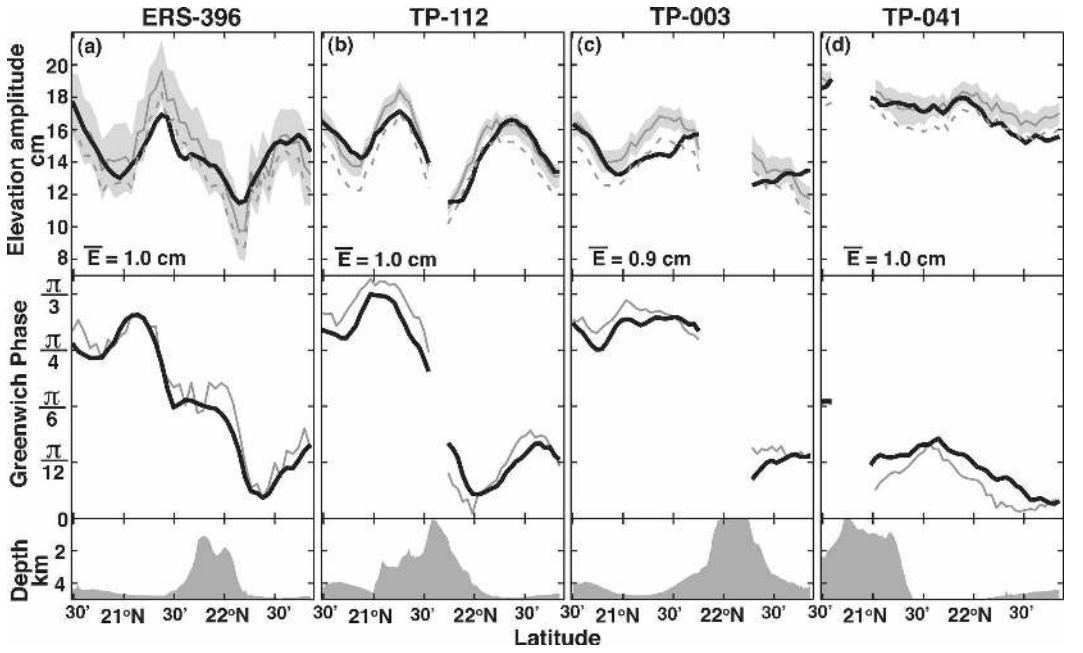

FIG. 3. Comparison of total M_2 surface elevation (barotropic plus baroclinic) from the model (black line) and from satellite altimetry (gray line). The location of the tracks are shown as gray lines in Fig. 2a. In the amplitude panels, the gray shading shows ± 1 standard error for the satellite amplitude measurements, and the dashed gray line is the satellite altimetry without the load tide correction.

surface elevation away from land, a comparison is made to the along-track M_2 fits of satellite altimetry data (Fig. 3). In addition to the three Ocean Topography Experiment (TOPEX)/Poseidon tracks (TP-003, TP-112, and TP-041) that cross the domain, we also consider data from the European Space Agency's European Remote Sensing Satellite (ERS; track 396), which goes though the middle of the Kauai Channel. The positions of the tracks are shown as gray lines in Fig. 2a. Overall, there is very good agreement in both amplitude and phase between our simulation and the satellite altimetry. Often the model lies within one standard error of the satellite data (Fig. 3, gray shading). The average RMSE along each track, $\overline{E} = n^{-1}\Sigma_n E$, ranges from 0.9 to 1.0 cm. The largest amplitude differences are on the order of 2 cm and occur at the first surface bounce along the ERS-396 track and around Kauai (TP-003).

This POM simulation, like the TPXO model from which the boundary conditions are derived, calculates the height of the ocean surface relative to the seabed. The satellite altimetry, however, gives the surface height relative to a reference geoid. The difference between these two measurements is the "load tide," the deformation of the solid earth due to the weight of the water above it. In the above comparisons, the satellite observations have had the load tide included using the TPXO6.2 load model. The dashed lines in the amplitude panels show the original (without load tide) satellite elevations. Inclusion of the load tide reduces $\overline{E}$ for TP-041 by 54%; for TP-112 by 26% and for ERS-396 by 2%; but it increases $\overline{E}$ for TP-003 by 10%. This is the first time, to our knowledge, that a process tide model has been shown to be accurate enough to require the load tide correction when validating to satellite data.

An intensive field experiment, the HOME Nearfield, which was conducted at Kaena Ridge from 2001 to 2003, resulted in detailed observations of the currents and mixing patterns. As a check on the validity of the model, we compare model output to M_2 harmonic fits from two moorings. One mooring, A2, was located on the southern edge of Kaena Ridge (Fig. 1, northern star) with three ADCPs giving coverage of most of the water column (Boyd et al. 2005). The second mooring, C2, was located south of the ridge in ~4000-m water depth (Fig. 1, southern star) with coverage only in the upper 700 m.

The magnitudes and vertical structure of the model amplitudes and phases agree well, for the most part, with the mooring observations (Fig. 4). The $\overline{E}$ range from 0.026 to 0.035 m s^{-1}. The largest amplitude differences are near the seafloor in A2 (Fig. 4a), where the model overpredicts both the u and v currents. An across-ridge section (not shown) indicates that the model predicts the formation of a near-bed downward-

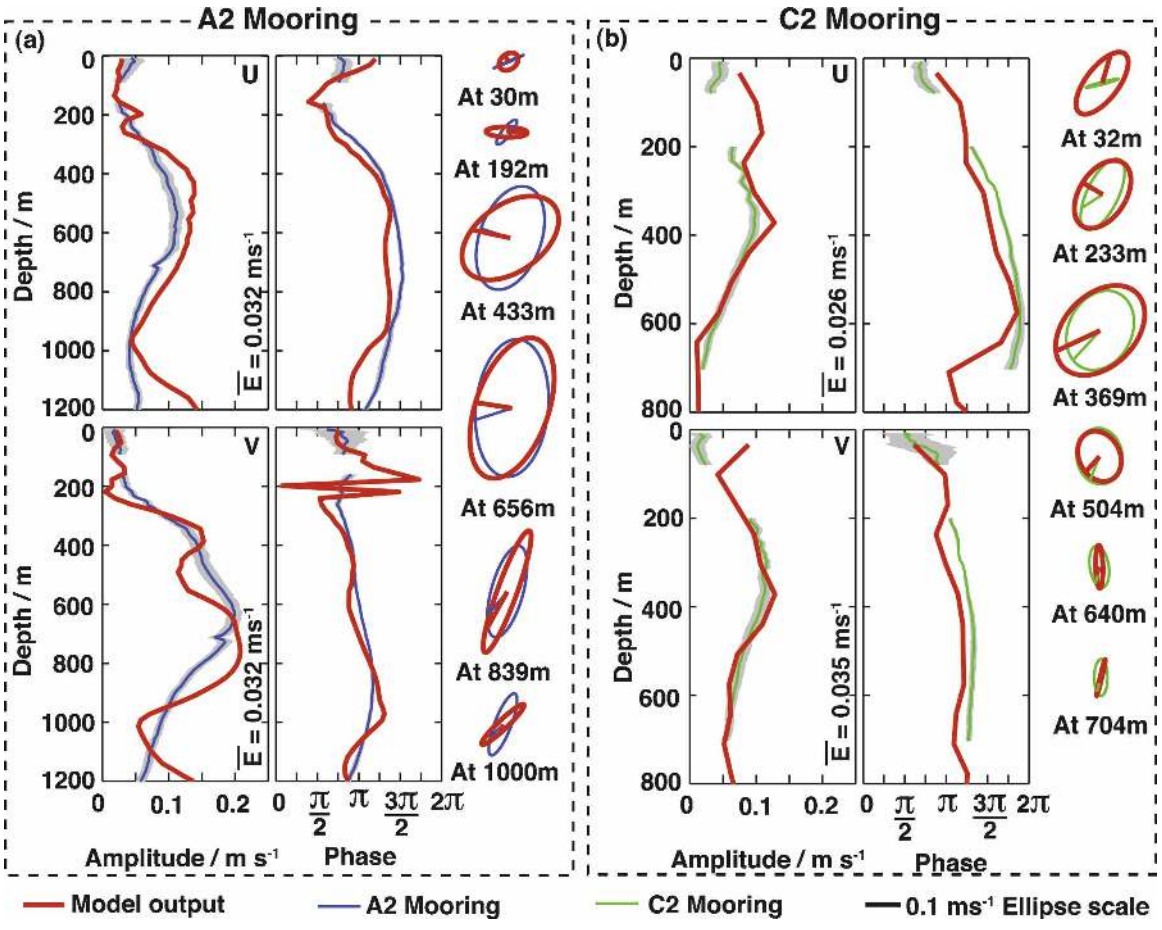

FIG. 4. Comparison of M_2 harmonic fits from the model and 5 months of moored ADCP data. (a) A2 mooring on the edge of the ridge crest; (b) C2 mooring south of the ridge. Ellipses are from depths where the model velocities were nearly collocated with ADCP observation.

propagating beam at A2. Such beams have been observed elsewhere on the Kaena Ridge (e.g., Nash et al. 2006; Aucan et al. 2006), but their formation is dependent on the criticality of the local slope (Balmforth et al. 2002; Garrett and Kunze 2007). It is possible that near A2 the 0.01° resolution topography is closer to critical than the actual topography.

At mooring C2, the model predicts a surface intensification in v velocity, which is not seen in the observations (Fig. 4b). Important near-surface forcing processes such as the wind and mesoscale activity are not included in this simulation and could easily alter the surface velocities. High-frequency radar observations at Kaena Ridge, taken as part of HOME, show that the M_2 surface velocity pattern predicted by the model is usually masked or altered by mesoscale processes (Chavanne 2007).

Current ellipses at depths where the model levels are nearly collocated with the ADCP measurements show good agreement at subsurface depths (Fig. 4). Near the surface, flows at both moorings are more rectilinear than predicted by the model.

Our ability to verify the simulation with the suite of observations described above gives us a high level of confidence in the model's ability to simulate the M_2 internal tide around the steep topography of the Hawaiian Islands. Including the baroclinic tide improves the prediction of the water level around the Hawaiian Islands. The RMSEs from the along-track satellite data ($\overline{E} \approx 1.0$ cm) are approximately one-third those for the barotropic M_2 TPXO model [Egbert and Erofeeva (2002) estimated the RMSE at 3.6 cm for ocean depths between 2500 and 4000 m, and Simmons et al. (2004) estimated it to be less than 3 cm over the entire domain].

c. *Modeled internal tide structure*

Although the focus of this work is on the energetics, it is constructive to briefly examine the structure of the internal tide generated at the Kaena Ridge. A transect

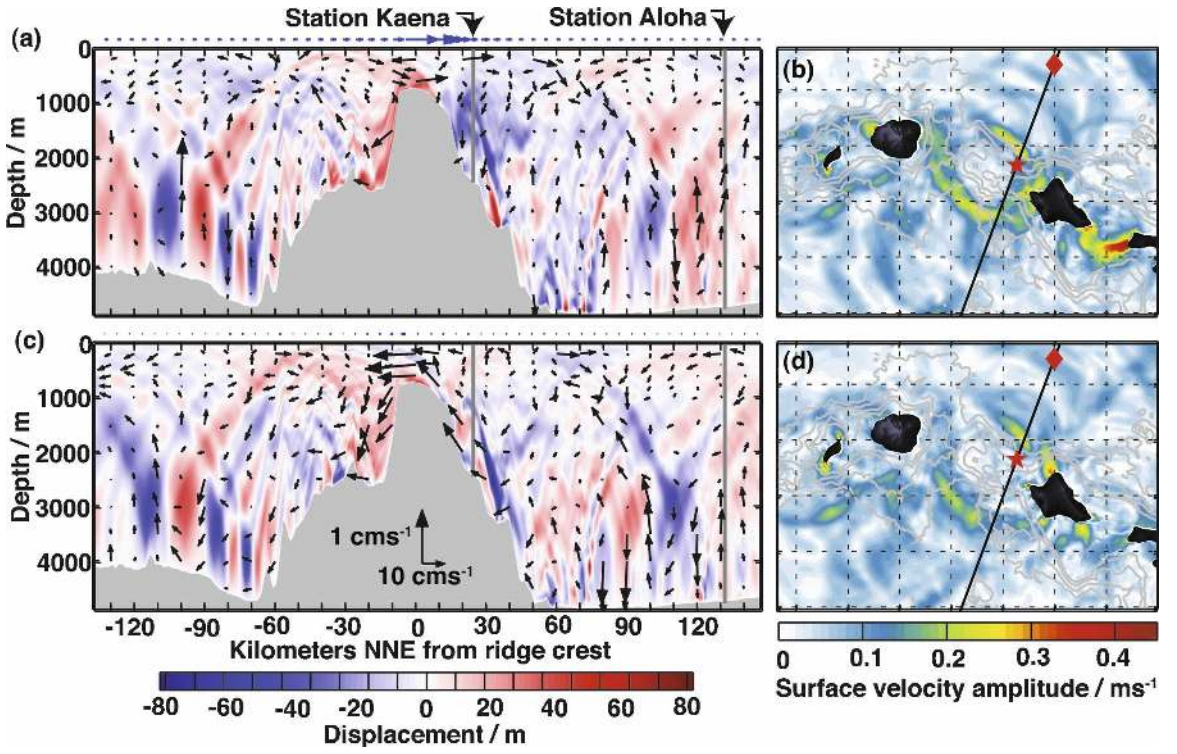

FIG. 5. The M_2 baroclinic currents (along section) and vertical displacement on a cross-ridge section through the HOT stations ALOHA and Kaena during (a) maximum north-northeast barotropic current and (c) 90° later during slack current. The vectors at the top of the two left-hand panels are the across-ridge barotropic currents. The total surface current (barotropic plus baroclinic) for the domain west of 157°W at (b) maximum north-northeast barotropic current and (d) 90° later during slack current. The black line shows the location of the section in (a) and (c). The diamond and star indicate the locations of Station ALOHA and Station Kaena, respectively.

across the ridge shows a complex vertical displacement and baroclinic current structure (Figs. 5a,c). Beamlike features emanate from the flanks of the ridge as well as from discontinuities deeper in the water column. This transect was chosen to pass through two stations occupied as part of the HOT experiment, including Station ALOHA where Chiswell (1994) observed internal tides from repeat hydrographic surveys. The structure is shown during maximum north-northeastward barotropic current (Fig. 5a) and the quadrature structure 3 h later during barotropic slack tide (Fig. 5c). Peak baroclinic currents (0.24 m s^{-1}) and displacements (92 m) are found along the tidal beams that originate on both sides of the ridge. During both plotted phases the displacement is upward on the south side and downward on the north side of the ridge. When the barotropic current slackens to near zero, 180° phase shifts of the baroclinic current occur in the beam, consistent with classic analytic descriptions of tidal beams (e.g., Rattray et al. 1969). The beams are more focused during maximum across-ridge barotropic flow than at slack flow.

The baroclinic energy flux (not shown) follows the same three main pathways seen in the vertical displacement: up and away from the ridge leading to surface bounces ~40 km on either side of the crest; up and over the top of the ridge, with beams crossing over the crest resulting in weaker fluxes; and down and away with some contact with the bottom along the near and supercritical slope. The crossing beams over the crest of the ridge have been described as a quasi-standing wave by Nash et al. (2006) and Carter et al. (2006). The downward-propagating beams have been examined in the context of near-boundary mixing by Aucan et al. (2006) and Aucan and Merrifield (2008).

The horizontal variability in the baroclinic structure can be assessed by considering the total (barotropic plus baroclinic) surface currents (Figs. 5b,d). The banding of higher velocity that parallels the ridge corresponds to the interaction of the beam with the surface mixed layer. The first surface bounce has velocities of ~0.2 m s^{-1}. Notice that near Station Kaena, this surface baroclinic current is comparable with the barotropic current over the ridge crest (Fig. 5a, blue arrows). Farther west, where the ridge crest is deeper, the baroclinic

surface currents associated with the surface bounce exceed the barotropic currents over the ridge crest (Fig. 5b). Overall, the strongest surface currents (up to 0.55 m s^{-1}) are barotropic and are found over the shallow Penguin Bank, southwest of Molokai.

3. Barotropic and baroclinic energy equations

To quantify how energy lost from the barotropic tide is distributed among barotropic and baroclinic processes, we develop and evaluate barotropic and baroclinic energy equations derived from POM's governing equations. In each equation, the energy is partitioned into tendency, flux divergence, nonlinear advection, barotropic-to-baroclinic conversion, and dissipation. The tendency, or time-varying component, would be zero for a perfectly steady-state solution. The conversion terms in the barotropic and baroclinic equations are derived independently but should be numerically similar as they represent the same process. The conversion term is a sink in the barotropic equation and a source in the baroclinic.

The energy equations, like the POM momentum equations, are in terms of sigma coordinates. The relationship between the z coordinate and the σ coordinate is

$$\sigma = \frac{z - \eta}{D}, \tag{2}$$

where η is the surface elevation, the seafloor is at $z = -H$, and the total depth of the water column is $D = H + \eta$. The horizontal velocity components are u and v; ω is the across-sigma-coordinate velocity. The vertical velocity is given by

$$w = \omega + u\left(\sigma\frac{\partial D}{\partial x} + \frac{\partial \eta}{\partial x}\right) + v\left(\sigma\frac{\partial D}{\partial y} + \frac{\partial \eta}{\partial y}\right) + \sigma\frac{\partial D}{\partial t} + \frac{\partial \eta}{\partial t}. \tag{3}$$

The density is decomposed into a constant, a depth-varying, and a perturbation component [i.e., $\rho_{\text{total}} = \rho_0 + \hat{\rho}(\sigma D + \eta) + \rho(x, y, \sigma, t)$]. Finally, because the bottom is not necessarily flat, we define the barotropic component, denoted by an overbar ($\bar{\ }$), to be the vertical average. The baroclinic component, denoted by a tilde ($\tilde{\ }$), is then taken to be the total minus barotropic.

The barotropic energy equation in $m^3\ s^{-3}$, with each term labeled for ease of reference, is

$$\begin{aligned}
&\text{Tendency} && D\frac{\partial}{\partial t}\left(\frac{\overline{u}^2 + \overline{v}^2}{2}\right) + \frac{\partial}{\partial t}\left(g\frac{\eta^2}{2}\right),\\
&\nabla\cdot\text{Flux} && + \frac{\partial}{\partial x}\left[D\overline{u}\left(g\eta + \frac{\overline{p}}{\rho_0}\right)\right] + \frac{\partial}{\partial y}\left[D\overline{v}\left(g\eta + \frac{\overline{p}}{\rho_0}\right)\right],\\
&\text{Advection} && + D\overline{u}\,\overline{\mathcal{A}_x'} + D\overline{v}\,\overline{\mathcal{A}_y'},\\
&\text{Conversion} && = -\frac{\overline{p}}{\rho_0}\frac{\partial \eta}{\partial t} + \frac{D\overline{u}}{\rho_0}\left[\frac{\partial \overline{p}}{\partial x} - \overline{g\int_\sigma^0\left(\frac{\partial \rho}{\partial x} - \sigma'\frac{1}{D}\frac{\partial D}{\partial x}\frac{\partial \rho}{\partial \sigma'}\right)D\,d\sigma'}\right]\\
&&& + \frac{D\overline{v}}{\rho_0}\left[\frac{\partial \overline{p}}{\partial y} - \overline{g\int_\sigma^0\left(\frac{\partial \rho}{\partial y} - \sigma'\frac{1}{D}\frac{\partial D}{\partial y}\frac{\partial \rho}{\partial \sigma'}\right)D\,d\sigma'}\right],\\
&\text{Dissipation} && + D\overline{u}(\overline{\mathcal{D}_x} + \overline{\mathcal{F}_x}) + D\overline{v}(\overline{\mathcal{D}_y} + \overline{\mathcal{F}_y}).
\end{aligned} \tag{4}$$

Similarly, the depth-integrated baroclinic energy equation is

$$\begin{aligned}
&\text{Tendency} && \int_{-1}^0 \frac{\partial}{\partial t}\left(\frac{\tilde{u}^2 + \tilde{v}^2}{2}\right)D\,d\sigma + \int_{-1}^0 \frac{g}{\rho_0}\left(-\frac{d\hat{\rho}}{dz}\right)^{-1}\frac{\partial}{\partial t}\frac{\rho^2}{2}\,D\,d\sigma,\\
&\nabla\cdot\text{Flux} && + \frac{1}{\rho_0}\frac{\partial}{\partial x}\int_{-1}^0 \tilde{u}\tilde{\rho}D\,d\sigma + \frac{1}{\rho_0}\frac{\partial}{\partial y}\int_{-1}^0 \tilde{v}\tilde{\rho}D\,d\sigma,\\
&\text{Advection} && + \int_{-1}^0 \tilde{u}\widetilde{\mathcal{A}_x}D\,d\sigma + \int_{-1}^0 \tilde{v}\widetilde{\mathcal{A}_y}D\,d\sigma + \int_{-1}^0 \frac{g}{\rho_0}\left(-\frac{d\hat{\rho}}{dz}\right)^{-1}\rho\widetilde{\mathcal{A}_\rho}D\,d\sigma,
\end{aligned}$$

$$\text{Conversion} = -\int_{-1}^{0} \frac{\tilde{p}}{\rho_0}\frac{\partial \omega}{\partial \sigma}\,d\sigma + \int_{-1}^{0} \frac{g}{\rho_0}\rho w D\,d\sigma - \int_{-1}^{0}\left[\frac{g}{\rho_0}\widetilde{\rho\sigma}\left(\tilde{u}\frac{\partial D}{\partial x} + \tilde{v}\frac{\partial D}{\partial y}\right) + \frac{g}{\rho_0}\tilde{\rho}\left(\tilde{u}\frac{\partial \eta}{\partial x} + \tilde{v}\frac{\partial \eta}{\partial y}\right)\right]D\,d\sigma,$$

$$\text{Dissipation} + \int_{-1}^{0} \tilde{u}(\widetilde{\mathcal{D}_x} + \widetilde{\mathcal{F}_x})D\,d\sigma + \int_{-1}^{0} \tilde{v}(\widetilde{\mathcal{D}_y} + \widetilde{\mathcal{F}_y})D\,d\sigma + \int_{-1}^{0} \frac{g}{\rho_0}\left(-\frac{d\tilde{\rho}}{dz}\right)^{-1}\rho(\mathcal{D}_\rho + \mathcal{F}_\rho)D\,d\sigma, \quad (5)$$

where g is gravitational acceleration and p is the perturbation pressure (calculated from the perturbation density). Here, $\mathcal{A}$, $\mathcal{D}$, and $\mathcal{F}$ denote the advection, vertical dissipation, and horizontal dissipation terms, respectively. The definition of these terms, along with the derivation of (4) and (5), are given in the appendix. These equations are evaluated at each time step and then averaged over an integer number of tidal periods. Note that as we are only advecting temperature and salinity in this study, $\mathcal{D}_\rho \equiv \mathcal{F}_\rho \equiv 0$.

This approach differs from previous numerical studies that have evaluated energy fluxes from harmonic fits to model time series (e.g., Cummins and Oey 1997; Merrifield and Holloway 2002). Equation (5) also emphasizes the difference between the barotropic-to-baroclinic conversion, which directly measures the work done by the barotropic tide on the baroclinic tide, and the baroclinic flux divergence, which measures radiated baroclinic energy. Merrifield and Holloway (2002) and Di Lorenzo et al. (2006) equated conversion to baroclinic flux divergence, thereby neglecting local baroclinic dissipation. Niwa and Hibiya (2001) calculate conversion from the harmonic fits as

$$c = \langle p'(-H)\cdot(\bar{\mathbf{u}}\cdot\nabla H)\rangle_\theta, \quad (6)$$

where $p'(z) = \int_z^0 N^2\zeta dz' - (1/H)\int_{-H}^0\int_z^0 N^2\zeta\,dz'\,dz$ is the perturbation pressure (Kunze et al. 2002), ζ is the isopycnal displacement, $\bar{\mathbf{u}}$ is the M_2 harmonic fit for the barotropic velocity, and $\langle\cdot\rangle_\theta$ indicates an average over a tidal cycle. In his Fig. 6, Katsumata (2006) schematically partitioned the energy into the same categories as used in (4) and (5), but he did not publish the equations. Zaron and Egbert (2006b), as part of a verification study, partitioned energy into reservoirs of kinetic and available potential energy.

4. Energy analysis

a. Energy balance

The terms of the barotropic and baroclinic energy equations [(4) and (5)] are averaged over the last 6 M_2 tidal cycles of an 18-tidal-cycle simulation. The area integrals presented in this section exclude the outer 12 cells along each boundary (20° 29.1′–22°53.1′N and 160°41.1′–155°29.7′W; gray line in Fig. 1). This exclusion is conservative, as there is no evidence that the effect of the relaxation layer extends beyond its 10-cell width (Carter and Merrifield 2007).

A total of 2.733 GW is lost from the barotropic tide within our domain (Table 2). The majority of this barotropic flux divergence is converted into baroclinic tides (2.286 GW), with the bottom friction (barotropic dissipation term) accounting for 0.163 GW. Of the energy converted from barotropic to baroclinic, 73% radiates out of the domain as baroclinic flux ($\nabla\cdot\text{Flux}_{\text{bc}} = 1.701$ GW). The majority of the remaining baroclinic energy is lost to dissipation within the domain (0.445 GW, 19%).

Although the simulation is forced only with M_2, nonlinear dynamics can transfer energy to higher harmonics (M_4, M_6, . . . ; e.g., Lamb 2004), to the subharmonic ($1/2M_2$, e.g., Carter and Gregg 2006), or into rectified tides. In (4) and (5), energy actively undergoing a nonlinear transformation would be in the advection term, whereas the tendency term includes the time rate of change of energy at all frequencies. The tendency and nonlinear advection terms are small in both the barotropic and baroclinic equations, suggesting little energy at, or being transferred to, other constituents. As the simulation started from a quiescent state, there was no "seed" energy at other frequencies to facilitate wave–wave interactions, and therefore, it is likely the nonlinear interactions are underestimated.

TABLE 2. Model barotropic and baroclinic energy estimates in gigawatts (GW; 10^9 W) integrated over the subdomain shown in Fig. 1. The sign of each term is consistent with its position in Eqs. (4) and (5). The error term is defined as the remainder after moving the terms to the left-hand side of (4) or (5) and summing.

	Tendency	$\nabla\cdot$ Flux	Advection	Conversion	Dissipation	Error
Barotropic	−0.006	−2.733	−0.005	−2.286	−0.163	−0.296
Baroclinic	+0.054	+1.701	+0.016	+2.340	−0.445	−0.125

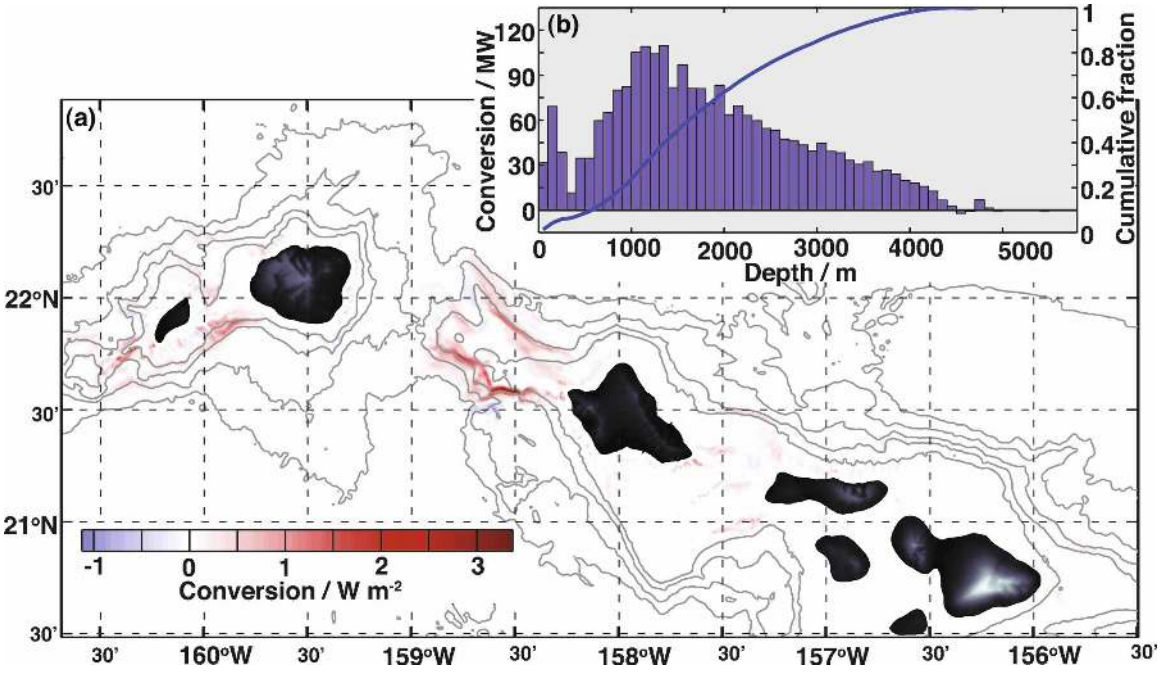

FIG. 6. (a) Map of barotropic-to-baroclinic conversion. The sign is consistent with it being a source term in the baroclinic equation. Contour interval is 1000 m. (b) Area integral of conversion term in 100-m depth bins and the cumulative fraction of conversion occurring in and above each depth bin.

The computational mode splitting technique can produce an erroneous energy source (Simmons et al. 2004; Zaron and Egbert 2006b). Simmons et al. (2004) found that with a ratio of eight or less barotropic iterations to one baroclinic iteration, the energy error was <10%, which they considered to not have a qualitative impact on their analysis. Our barotropic error term is 10.8% of the flux divergence (−0.296 GW), which we attribute to the 50:1 mode split used in the present simulation. The baroclinic error is 5.3% of the conversion term, twice the difference between the two estimates of conversion (2.4%).

A 30 M_2 tidal-cycle simulation was performed to check the stability of the 18 tidal- cycle results. As in the 18-tidal-cycle simulation, the energy analysis was performed over the last 6 tidal cycles. The flux divergence and conversion values changed by $\lesssim$1% in both the barotropic and baroclinic balances. The absolute differences in dissipation were similar, 0.01–0.03 GW, which because of their small initial values results in differences of 3%–7%.

Sigma coordinate models such as POM generate erroneous currents through a pressure-gradient error (e.g., Mellor et al. 1994). In this simulation we observed these zero-frequency currents to be layered throughout the water column with the layers having opposite sign, such that they cancel in the vertical integral. Being zero frequency, they are excluded from the harmonic fits, so a further check on (4) and (5) is obtained by calculating the conversion from the harmonic fits using (6). This approach gives 2.368 GW of conversion, which is larger than our baroclinic value by only 1.2%. The mean and standard deviation of the RMS differences between the barotropic model output and the corresponding harmonic time series are (1.5, 0.8) mm, (2.0, 5.5) mm s^{-1}, and (1.9, 4.8) mm s^{-1} for η, $\bar{u}$, and $\bar{v}$, respectively. Only the barotropic field time series could be stored because of file size constraints. The largest departures from sinusoidal (RMS differences) occur near headlands on Oahu and Molokai (not shown). Therefore we conclude that non-M_2 currents, both physical (M_4, M_6, . . .) and erroneous, have little effect on the regional energy balances.

b. Structure of baroclinic energy fields

The ~2.3 GW lost to internal tides in the barotropic energy balance becomes the source term in the baroclinic balance. The barotropic-to-baroclinic conversion occurs mainly on both sides of the Kaena Ridge, northwest of Oahu, and south of the 1000-m isobath surrounding Kauai and Niihau (Fig. 6a). The M_2 conversion is weak in the Kaiwi Channel (between Oahu and Molokai), although conversion occurs off Makapuu, the eastern tip of Oahu. Very little conversion occurs east

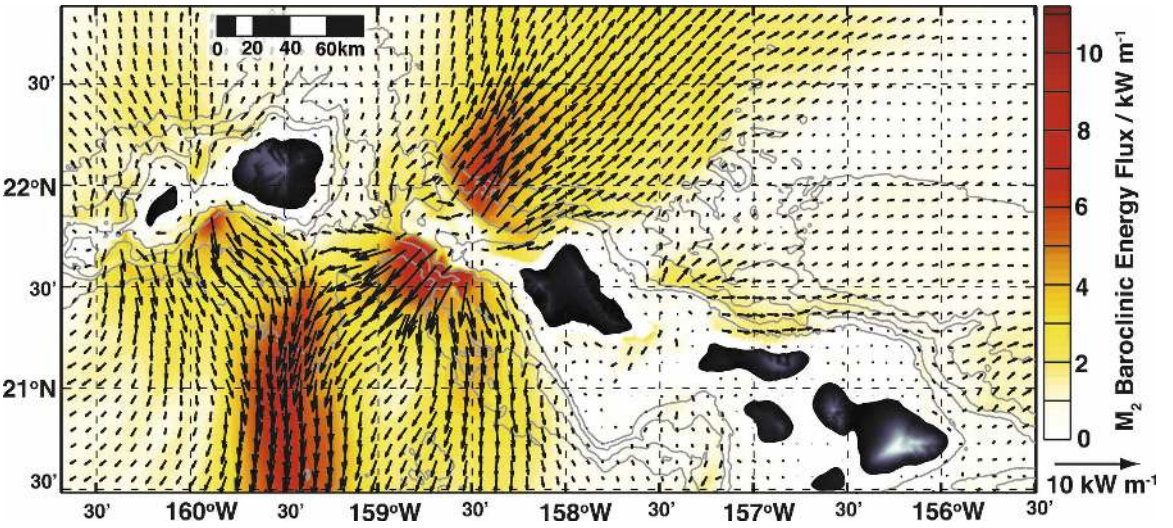

FIG. 7. Depth-integrated M_2 baroclinic energy flux vectors. Every eighth vector in each direction has been plotted. The underlying color gives the flux magnitude. Contour interval is 1000 m.

of 157°W. Forty percent of the internal tide generation occurs between the 1000- and 2000-m isobaths, and 84% occurs over topography shallower than 3000 m (Fig. 6b).

From these generation sites, baroclinic energy radiates away from the ridge (Fig. 7). The largest fluxes are contained within two beams: one propagating northeast from the Kaena Ridge, and another southward beam formed from the interaction of the Niihau and Kaena generation sites. The broad dimensions of these beams are set by the length of the generation region; as such, similar features are seen in the coarser simulations of Merrifield and Holloway (2002) and Simmons et al. (2004). The global simulations of Simmons et al. (2004) show that in the absence of mesoscale disturbances these beams are coherent for large distances. The details and magnitude of the fluxes are, however, dependent on the slope and resolution of the topography.

Small-scale structures are observed emanating from localized generation regions. A second, southward beam occurs as a result of fluxes from the near-Oahu end of Kaena Ridge being steered by the topography south of Oahu. North of Molokai there is a ~30-km wide beam parallel to the isobaths, and the generation off Makapuu Point leads to baroclinic energy fluxes that are steered around the south shore of Oahu. The smooth transitions between the flux regions are likely due to the linearity of the solutions (section 4a) as well as low numerical noise.

The rate of turbulent baroclinic energy loss within the model (Fig. 8) is a combination of the MY2.5 submodel (κ_m) and the Smagorinsky horizontal diffusivity (A_M). These quantities enter (5) through the $\mathcal{D}_x$, $\mathcal{D}_y$, and $\mathcal{F}_x$, $\mathcal{F}_y$ terms, respectively. The total amount of vertical (submodel) mixing appears to be partly dependent on how noisy the simulation is, and in our simulations, the vertical mixing from the submodel is less than expected from observations. However, the combined horizontal and vertical baroclinic dissipation is consistent with the observed diapycnal mixing. From microstructure observations at a small seamount on the Kaena Ridge (21°43.8′N, 158°38.8′W), Carter et al. (2006) found an average turbulent dissipation rate of $\bar{\varepsilon} = 6.2 \times 10^{-8}$ W kg^{-1}. If averaged over the water column $\bar{\varepsilon}\rho_0 D$, where D = 1000 m and ρ_0 = 1025 kg m^{-3}, this would be $\sim 10^{-1}$ W m^{-2}, similar to the modeled dissipation in that location. A more detailed comparison to microstructure observations is included in the next section.

c. Energy terms with distance from ridge

In this section we consider how the energy varies with distance from the ridge crest. As can be seen from Table 2, the baroclinic energy balance is predominately between three terms:

$$\nabla \cdot \text{Flux} = \text{Conversion} - \text{Dissipation}. \qquad (7)$$

We integrate these terms over regions bounded by the 1000-, 2000-, and 3000-m isobaths, as well as lines paralleling the 3000-m isobath at distances of 10, 20, 30, 40, 60, 80, 100, and 120 km (Fig. 9a). Each region is further divided into north and south by a line that passes through the main islands (Fig. 9a, heavy line).

The total southward flux peaks 10 km beyond the 3000-m isobath with a value of 0.95 GW (Fig. 9b). The northward flux is weaker (maximum of 0.84 GW) and

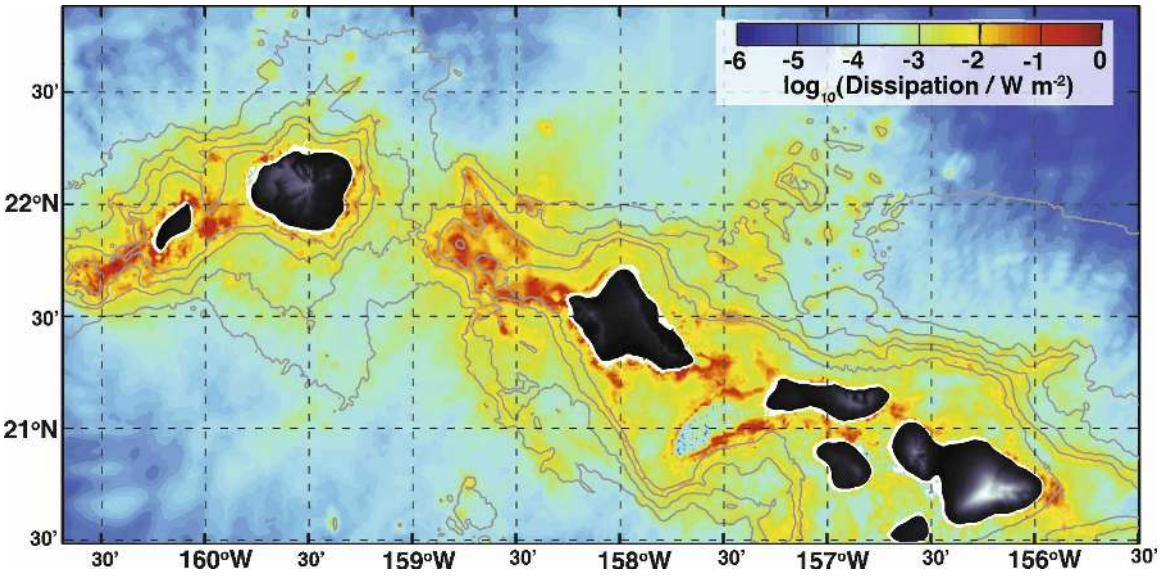

FIG. 8. Map of depth-integrated baroclinic dissipation from the model. This includes both vertical $[\int_{-1}^{0} (\tilde{u}\widetilde{\mathcal{D}_x} + \tilde{v}\widetilde{\mathcal{D}_y})\, d\sigma]$ and horizontal $[\int_{-1}^{0} (\tilde{u}\widetilde{\mathcal{F}_x} + \tilde{v}\widetilde{\mathcal{F}_y})\, d\sigma]$ contributions. As we are only advecting temperature and salinity, $\mathcal{D}_\rho \equiv \mathcal{F}_\rho \equiv 0$. Contour interval is 1000 m.

peaks farther from the ridge, at a distance of 30 km from the 3000-m isobath. After peaking, the flux slowly decays with distance from the ridge. The flux 120 km from the 3000-m isobath is 3% (6%) lower than the maximum on the north (south) side of the ridge. However, it is not always possible to be within the model domain at 120 km from the 3000-m isobath (particularly south of the ridge); consequently, these flux decays are an overestimate.

The area-integrated conversion, baroclinic flux divergence, and dissipation are all larger on the south side of the ridge (Fig. 9c). Most of the conversion (and flux divergence) occurs within 10 km of the 3000-m isobath, in agreement with the analysis presented in Fig. 6b. In most regions, the conversion is slightly larger than the flux divergence, resulting in small dissipation. The exception is within the southern portion of the 1000-m isobath where the dissipation exceeds the flux divergence by 18.8 MW.

Thirty percent (132 out of 445 MW) of the total baroclinic dissipation in the model occurs within the 1000-m isobath south of the ridge crest. Of that 64.5 MW is dissipated between 158°12′ and 157°00′W, which encompasses Oahu minus Kaena Point through to the middle of Molokai. The majority of the relatively small amount of generation that occurs in this region is confined off Makapuu Point (Fig. 6a). The depth-integrated flux vectors (Fig. 10) show that the internal tide generated at Makapuu Point tends to either follow the coastline around into Mamala Bay (previously studied by Eich et al. 2004; Alford et al. 2006; Martini et al. 2007) or head south and be dissipated along the edge of Penguin Bank. In either case, very little of the internal tide energy generated here crosses the 1000-m isobath. Not only does this contrast sharply with the majority of the generation sites where most of the energy radiates significant distances but it means that 14% of the dissipation within the domain comes from a generation region with no radiative signature.

As part of the HOME Nearfield experiment, a total of 313 microstructure profiles were taken over topography less than 1000 m deep on the Kaena Ridge (Fig. 11). The data were collected with the loosely tethered deep Advanced Microstructure Profiler (AMP), which evaluates ε from centimeter-scale shear variance (Osborn and Crawford 1980; Gregg 1987; Wesson and Gregg 1994). These data allow a comparison between the modeled baroclinic dissipation and field observations. The AMP profiles were integrated over the water column from a 22-m depth (to avoid contamination from the ship) to ~20 m above the bed (where profiling was stopped to avoid damaging the instrument on the rough volcanic seabed). The profiles were then binned according to bottom depth with a bin interval of 100 m; for example, all profiles taken over topography between 100 and 200 m deep were grouped together. The profiles within each bin were then bootstrap averaged and multiplied by the area associated with that depth range (with the eastern boundary being 158°12′W). The area-integrated dissipation was 28 MW with a 95% confidence interval of 17–42 MW.

The modeled baroclinic dissipation within the

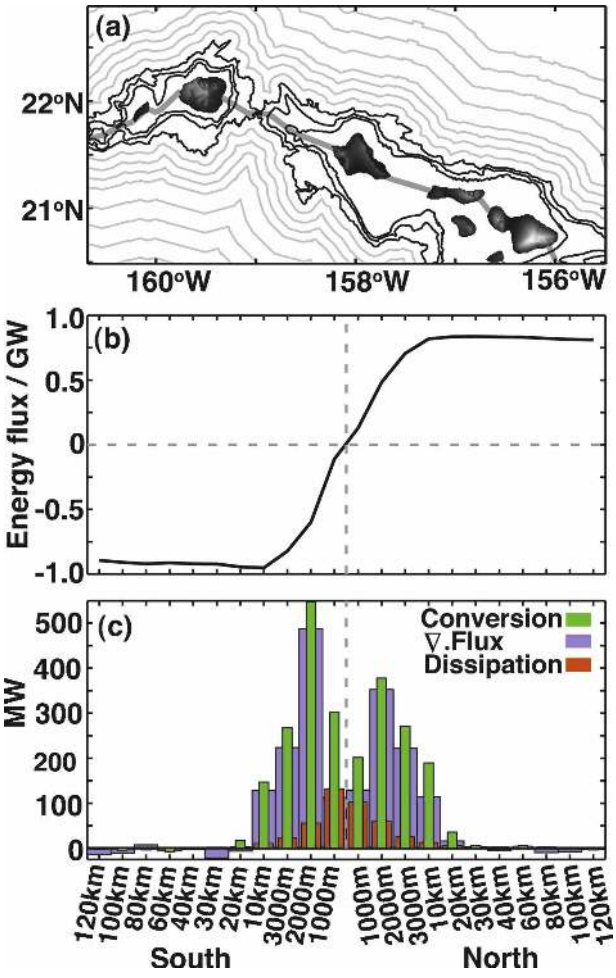

FIG. 9. (a) Boundaries of the regions used for assessing the energy as a function of distance from the ridge crest. The lines are the 1000-, 2000-, and 3000-m isobaths, and lines paralleling the 3000-m isobath at distances of 10, 20, 30, 40, 60, 80, 100, and 120 km. The heavy line divides the regions into north and south. (b) Net baroclinic energy flux calculated by integrating flux divergence out to the lines given in the top panel. (c) Conversion, flux divergence, and dissipation within the regions defined by the lines in the top panel.

1000-m isobath for the Kaena Ridge west of 158°12′W is 48.7 MW. This is above the upper limit of the 95% confidence interval on the area-weighted observations but within a factor of 2 of the observed mean (28 MW). A factor of 2 is often taken as the threshold for determining equivalence between ε measurements (Osborn 1980; Oakey 1982; Carter and Gregg 2002), so we consider this acceptable agreement between the modeled dissipation and the microstructure. It should be noted that the microstructure observations include dissipation of energy from all sources, not just M_2 tides. However, M_2 is the dominant tidal frequency in this region, both in terms of barotropic velocity (Carter et al. 2006) and

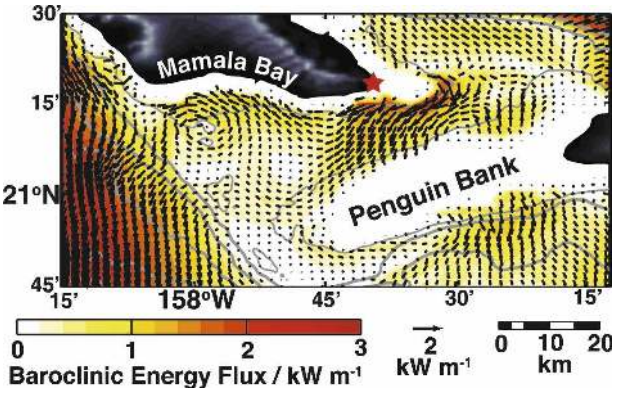

FIG. 10. Depth-integrated M_2 baroclinic energy flux vectors for the region around Makapuu Point (marked with the red star). Every second vector in each direction has been plotted. The underlying color gives the flux magnitude. The line contours are at 500-m depth, and the thicker contours are at intervals of 1000 m.

barotropic-to-baroclinic conversion (Zaron and Egbert 2006a). The limited depth range used in the microstructure integration helps minimize the effect of surface and bottom boundary mixing on the comparison.

5. Comparison to Merrifield and Holloway

The model results presented in Merrifield and Holloway (2002) were used extensively in both the planning and analysis of the HOME field observations (e.g., Rudnick et al. 2003; Klymak et al. 2006; Lee et al. 2006). They divided the Hawaiian Ridge into five subdomains (Fig. 12, black lines). Their simulations used 4-km-resolution grids derived from Smith and Sandwell (1997) bathymetry, compared to the 0.01° (~1 km) multibeam-derived grid used in the current analysis. In this section, we revisit some of the findings from Merrifield and Holloway (2002).

The small decrease in flux divergence that we find

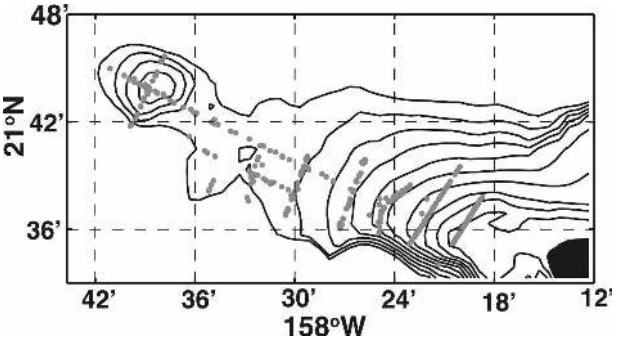

FIG. 11. Location of AMP microstructure profiles taken over Kaena Ridge as part of the HOME Nearfield experiment. The contour interval is 100 m.

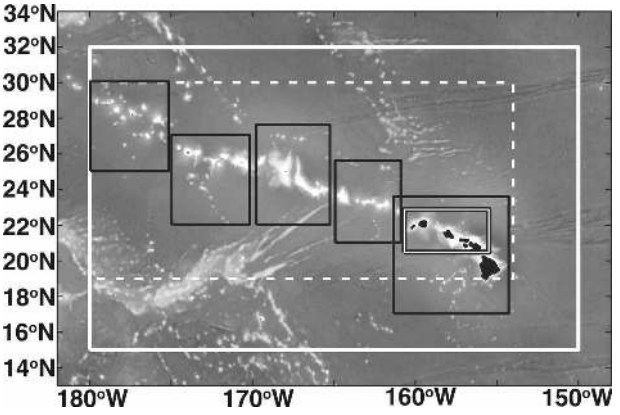

FIG. 12. The extent of the current model domain compared to domains used in previous estimates of conversion at the Hawaiian Ridge. The current model is marked by the black-white-black line. The solid white line is used by Zaron and Egbert (2006a); the dashed line by Niwa and Hibiya (2001); and the solid black lines shows the five regions used in Merrifield and Holloway (2002), numbered from right to left.

occurs off the ridge (Fig. 9b) contrasts with the ~0.5 GW (100 km)$^{-1}$ decay rate reported by Merrifield and Holloway (2002). There appears to be two factors that contribute to their overestimate of energy flux decay. First, the integration time in their simulations was very short, only 4 days, which does not allow the higher modes to propagate throughout the domain. Carter and Merrifield (2007) plot energy flux from a ridge versus distance for a range of integration times, and the shape of the curves where the higher modes have not reached the boundary are similar to those shown by Merrifield and Holloway (2002). Second, Merrifield and Holloway (2002) calculate the energy flux by "integrating the ridge normal component of the energy flux density vector", that is,

$$f_1(x) = \int_{y_2}^{y_1} \mathbf{F}(x, y')\, dy', \tag{8}$$

where the domain has been rotated so the ridge lies in the x direction. Unlike the area integral used in Fig. 9, this approach does not account for radial spreading and energy leaving through the side of the box.

The magnitude of modeled internal tide generation is sensitive to topographic resolution (Di Lorenzo et al. 2006; N. V. Zilberman et al. 2008, unpublished manuscript). In particular, the barotropic-to-baroclinic conversion is reduced for a coarser grid or when the underlying bathymetry is smoothed. To assess the effect of the higher-resolution topography on generation around Hawaii, we conducted an 18 M_2 tidal- cycle simulation using the same 4-km-resolution, Smith and Sandwell (1997) topography-derived grid that Merrifield and Holloway (2002) used for their region 1. Equation (6) then gives the generation[2] over a subregion corresponding to the 0.01° domain, as 1.843 GW. This is 19%–22% lower than the corresponding conversion values from Table 2 or from (6) applied to the current simulation. Limited computing resources do not allow us to run our domain at any finer resolution at this time, and therefore we cannot be sure that ~1-km resolution is sufficient for the internal tide generation to converge.

Merrifield and Holloway (2002) do not directly calculate internal tide generation, but rather they estimate it from integrating the flux divergence over regions shallower than 4000 m deep. This approach excludes baroclinic energy that is generated and dissipated within the integration region. Integrating the 4-km flux divergence over the region of the high-resolution model gives 1.380 GW; that is, Merrifield and Holloway (2002) underestimate generation by ~40% compared to Table 2.

By assuming that the 4-km flux divergence underestimates the generation over the Hawaiian Ridge as it does between Niihau and Maui, it is possible to extrapolate our results to the entire Merrifield and Holloway (2002) domain. Scaling their estimated 10.2 GW up by 40% gives 14.3 GW of barotropic-to-baroclinic conversion. Niwa and Hibiya (2001) applied (6) to a 1/16° (~7 km) resolution primitive equation simulation and found ~15 GW of conversion for the region bounded by the white dashed line in Fig. 12. Recall that we found that (6) applied to a 4-km-resolution model underestimated conversion from (4) and (5) by ~20%. Assuming that underestimation for the 1/16° resolution model is at least as large, then the revised conversion value would be ≳18 GW. The difference between the estimates from extrapolating Merrifield and Holloway (2002) and Niwa and Hibiya (2001) may be due to different size domains, in particular, conversion occurring in the gaps between the Merrifield and Holloway (2002) subdomains.

Zaron and Egbert (2006a), using a 2D satellite altim-

[2] Both the Merrifield and Holloway (2002) simulation and our rerun of that grid contain significantly more cell-to-cell numerical noise than the ~1-km simulation presented in this paper. This is primarily because of the different scales of the underlying datasets [Smith and Sandwell (1997) is much coarser than multibeam], and hence the 4-km grid cannot be considered smoother than the current grid. This numerical noise affects the energy calculation of (4) and (5). The baroclinic conversion and dissipation terms were most effected by the noise. Consequently, we use (6) here to estimate the generation.

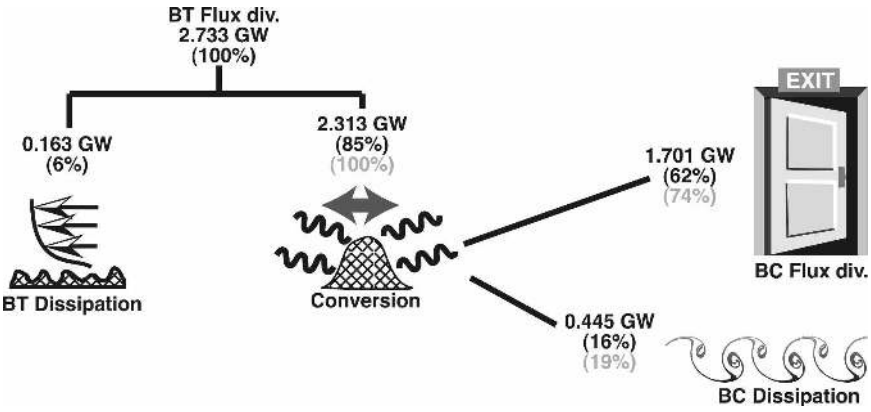

FIG. 13. Cartoon summarizing the major components to the M_2 tidal energy budget in the model. The percentages given in black are relative to the energy lost from the barotropic tide, and those in gray are relative to the barotropic-to-baroclinic conversion. The conversion value used is the average of the two estimates in Table 2.

etry–constrained inverse model, estimate 19 GW of M_2 barotropic flux divergence over the Hawaiian Ridge (Fig. 12, solid white line). Based on our findings (Table 2), 84% of this (16 GW) goes into internal tides. This lies between the scaled estimates of Merrifield and Holloway (2002) and Niwa and Hibiya (2001).

6. Summary and discussion

A 0.01°–horizontal resolution primitive equation (Princeton Ocean Model) simulation is used to derive an M_2 energy budget for the region from Niihau to Maui. This domain includes the Kaena Ridge, which had been previously identified as one of the main sites of barotropic-to-baroclinic conversion along the Hawaiian Ridge. The simulation was found to have a high level of skill when validated against satellite and in situ sea level observations, currents from moored ADCPs, and even microstructure measurements. RMSEs comparing the simulation to M_2 harmonic fits from data were $\lesssim$1 cm compared to sea level, and $\sim$0.035 m s^{-1} for moored velocity observations. The modeled baroclinic dissipation [a combination of Mellor and Yamada (1982) vertical mixing and Smagorinsky horizontal diffusivity] agrees to within a factor of 2 with the area-weighted integral of 313 microstructure profiles taken over the Kaena Ridge. To our knowledge, this is the most direct comparison of microstructure data to an internal tide process model yet.

Barotropic and baroclinic energy equations were derived from POM's governing equations. Of the 2.7 GW lost from the barotropic tide, 163 MW is dissipated by bottom friction and 2.3 GW is converted into internal tides. The majority of the internal tide energy (1.7 GW) is radiated out of the model domain, while 0.45 GW is dissipated close to the generation regions. Figure 13 gives a schematic summary of this M_2 energy pathway. Note that 16% of the barotropic flux divergence that is lost to baroclinic dissipation compares well to the $\sim$15% found by Klymak et al. (2006) from an extrapolation of microstructure observations to the entire Hawaiian Ridge. The 74% of baroclinic energy radiated out of the domain is consistent with the analytical work of St. Laurent and Garrett (2002), who found that less than 30% of the energy flux is generated at smaller spatial scales and may be available to dissipate locally.

An interesting exception to the general rule that the vast majority of the baroclinic energy radiates away is that almost all of the internal tide generated at Makapuu (southeast tip of Oahu) is dissipated within the 1000-m isobath. This small generation site accounts for 14% of the baroclinic dissipation within the domain. We postulate that other such regions, where local dissipation $\approx$ conversion, must exist in the global ocean and hence may play a role in global energy budgets.

We find that by equating conversion to flux divergence at the 4000-m isobath and using Smith and Sandwell (1997)–derived, 4-km-resolution topography, Merrifield and Holloway (2002) underestimated barotropic-to-baroclinic conversion by $\sim$40% compared to the 1-km resolution, multibeam-derived bathymetry used in the present study. Further, applying the energy Eqs. (4) and (5) to the coarser Merrifield and Holloway (2002) model grid still underestimates conversion by $\sim$20% compared to our simulation. This indicates that a detailed energy budget for the entire Hawaiian Ridge will require multibeam-derived bathymetry over a much larger area than currently available.

Acknowledgments. The bathymetry data were provided and gridded to 0.01° by Paul Johnson of the Hawaii Regional Mapping Group. We thank Jerome Aucan, Kevin Bartlett, Cedric Chavanne, Thomas Decloedt, Walt Waldorf, Nathalie Zilberman, and the crew of the R/V *Wecoma* for assistance with the mooring data. The microstructure data were collected with the assistance of Matthew Alford, Paul Aguilar, Steve Bayer, Earl Krause, John Mickett, Jack Miller, Avery Synder, Maya Whitmont, Dave Winkel, and the crew of the R/V *Revelle*. Richard Ray kindly provided the harmonic fits to the along-track satellite data. The authors thank two anonymous reviewers.

This work was funded by the National Science Foundation (NSF) Grant OCE0425347. The microstructure and moored current data employed in this paper were collected as part of the Hawaii Ocean Mixing Experiment. The microstructure data collection was supported by NSF Grants OCE9818693 and OCE9819535 to M. Gregg and J. Miller at the University of Washington; the mooring data collection was supported by NSF Grant OCE9819533 to D. Luther and M. Merrifield at the University of Hawaii, and Grant OCE9819532 to M. Levine and T. Boyd at Oregon State University. The temperature and salinity data from Station ALOHA were supplied by the HOT program (NSF Grants OCE9303094, 0117919, and 0327513).

APPENDIX

Derivation of Energy Equations

Here we outline the derivation of the barotropic and baroclinic energy equations presented above. Using the definitions from section 3, the hydrostatic and Boussinesq equations of motion in σ coordinates are

$$\frac{\partial u}{\partial t} + \mathcal{A}_x - fv = -g\frac{\partial \eta}{\partial x} - \frac{1}{\rho_0}\frac{\partial p}{\partial x} - \frac{\rho}{\rho_0}g\left(\sigma\frac{\partial D}{\partial x} + \frac{\partial \eta}{\partial x}\right) + \mathcal{D}_x + \mathcal{F}_x, \tag{A1}$$

$$\frac{\partial v}{\partial t} + \mathcal{A}_y + fu = -g\frac{\partial \eta}{\partial y} - \frac{1}{\rho_0}\frac{\partial p}{\partial y} - \frac{\rho}{\rho_0}g\left(\sigma\frac{\partial D}{\partial y} + \frac{\partial \eta}{\partial y}\right) + \mathcal{D}_y + \mathcal{F}_y, \tag{A2}$$

$$\frac{\partial \eta}{\partial t} + \frac{\partial (uD)}{\partial x} + \frac{\partial (vD)}{\partial y} + \frac{\partial \omega}{\partial \sigma} = 0, \quad \text{and} \tag{A3}$$

$$\frac{\partial \rho}{\partial t} + \mathcal{A}_\rho = -w\frac{\partial \hat{\rho}}{\partial z} + \mathcal{D}_\rho + \mathcal{F}_\rho, \tag{A4}$$

where the advection terms are

$$\mathcal{A}_x = \mathbf{u}\cdot\nabla u + \frac{\omega}{D}\frac{\partial u}{\partial \sigma}, \tag{A5}$$

$$\mathcal{A}_y = \mathbf{u}\cdot\nabla v + \frac{\omega}{D}\frac{\partial v}{\partial \sigma}, \quad \text{and} \tag{A6}$$

$$\mathcal{A}_\rho = \mathbf{u}\cdot\nabla \rho + \frac{\omega}{D}\frac{\partial \rho}{\partial \sigma}, \tag{A7}$$

and the vertical and horizontal dissipative terms are

$$\mathcal{D}_x = \frac{1}{D}\frac{\partial}{\partial \sigma}\left(\frac{\kappa_m}{D}\frac{\partial u}{\partial \sigma}\right), \tag{A8}$$

$$\mathcal{D}_y = \frac{1}{D}\frac{\partial}{\partial \sigma}\left(\frac{\kappa_m}{D}\frac{\partial v}{\partial \sigma}\right), \tag{A9}$$

$$\mathcal{F}_x = \frac{1}{D}\left\{\frac{\partial}{\partial x}\left(2A_M H\frac{\partial u}{\partial x}\right) + \frac{\partial}{\partial y}\left[A_M H\left(\frac{\partial u}{\partial y} + \frac{\partial v}{\partial x}\right)\right]\right\}, \quad \text{and} \tag{A10}$$

$$\mathcal{F}_y = \frac{1}{D}\left\{\frac{\partial}{\partial x}\left[A_M H\left(\frac{\partial u}{\partial y} + \frac{\partial v}{\partial x}\right)\right] + \frac{\partial}{\partial y}\left(2A_M H\frac{\partial v}{\partial y}\right)\right\}. \tag{A11}$$

Here, A_M is the horizontal kinematic viscosity

$$A_M = c\frac{\Delta x \Delta y}{2}\sqrt{\left(\frac{\partial u}{\partial x}\right)^2 + \left(\frac{\partial v}{\partial x} + \frac{\partial u}{\partial y}\right)^2 + \left(\frac{\partial v}{\partial y}\right)^2}, \tag{A12}$$

and κ_m is the vertical eddy diffusivity from the Mellor and Yamada (1982) submodel. The surface and bottom boundary conditions on $\kappa_m/D(\partial u/\partial\sigma, \partial v/\partial\sigma)$ are given by the surface wind stress and bottom frictional stress, respectively (Blumberg and Mellor 1987). Finally, we do not provide explicit definitions of the vertical and horizontal dissipation terms ($\mathcal{D}_\rho$ and $\mathcal{F}_\rho$), as these terms are identically zero in our analysis because temperature and salinity are only advected.

For the barotropic energy equation, we recast the

momentum equations [(A1) and (A2)] to take advantage of the pressure-gradient variables calculated by the model (Blumberg and Mellor 1987; Mellor 2004):

$$\frac{\partial(uD)}{\partial t} + \frac{\partial(u^2D)}{\partial x} + \frac{\partial(uvD)}{\partial y} + \frac{\partial(u\omega)}{\partial \sigma} - fvD + gD\frac{\partial \eta}{\partial x} + D\frac{g}{\rho_0}\int_\sigma^0 \left(D\frac{\partial \rho}{\partial x} - \sigma'\frac{\partial D}{\partial x}\frac{\partial \rho}{\partial \sigma'}\right) d\sigma' = D(\mathcal{D}_x + \mathcal{F}_x) \quad \text{and} \tag{A13}$$

$$\frac{\partial(vD)}{\partial t} + \frac{\partial(uvD)}{\partial x} + \frac{\partial(v^2D)}{\partial y} + \frac{\partial(v\omega)}{\partial \sigma} + fuD + gD\frac{\partial \eta}{\partial y} + D\frac{g}{\rho_0}\int_\sigma^0 \left(D\frac{\partial \rho}{\partial y} - \sigma'\frac{\partial D}{\partial y}\frac{\partial \rho}{\partial \sigma'}\right) d\sigma' = D(\mathcal{D}_y + \mathcal{F}_y). \tag{A14}$$

We define the σ average as

$$\overline{(\cdot)} \equiv \int_{-1}^{0} (\cdot)\, d\sigma.$$

The σ-averaged form of (A13), denoted $\overline{(A13)}$, then becomes

$$\frac{\partial \overline{u}}{\partial t} + \overline{\mathcal{A}'}_x - f\overline{v} = -g\frac{\partial \eta}{\partial x} - \frac{g}{\rho_0}\overline{\int_\sigma^0 \left(D\frac{\partial \rho}{\partial x} - \sigma'\frac{\partial D}{\partial x}\frac{\partial \rho}{\partial \sigma'}\right) d\sigma'} + \overline{\mathcal{D}_x} + \overline{\mathcal{F}_x},$$

where

$$\overline{\mathcal{A}'_x} = \overline{u}\frac{\partial \overline{u}}{\partial x} + \overline{v}\frac{\partial \overline{u}}{\partial y} + \frac{1}{D}\left\{\frac{\partial}{\partial x}[D(\overline{u^2} - \overline{u}^2)] + \frac{\partial}{\partial y}[D(\overline{uv} - \overline{u}\,\overline{v})]\right\}.$$

The σ-averaged continuity equation, denoted $\overline{(A3)}$, is

$$\frac{\partial \eta}{\partial t} + \frac{\partial \overline{u}D}{\partial x} + \frac{\partial \overline{v}D}{\partial y} = 0.$$

The barotropic energy Eq. (4) is then obtained by evaluating

$$D\overline{u}\,\overline{(A13)} + D\overline{v}\,\overline{(A14)} + \left(g\eta + \frac{\overline{p}}{\rho_0}\right)\overline{(A3)}.$$

The baroclinic component is formed by subtracting the σ average from (A1) to (A4). For example, $\widetilde{(A1)} = (A1) - \overline{(A1)}$:

$$\frac{\partial \tilde{u}}{\partial t} + \widetilde{\mathcal{A}_x} - f\tilde{v} = -\frac{1}{\rho_0}\frac{\partial \tilde{p}}{\partial x} - \frac{g}{\rho_0}\left(\widetilde{\rho\sigma}\frac{\partial D}{\partial x} + \tilde{\rho}\frac{\partial \eta}{\partial x}\right) + \widetilde{\mathcal{D}_x} + \widetilde{\mathcal{F}_x},$$

noting that $\widetilde{\mathcal{A}_x} = \mathcal{A}_x - \overline{\mathcal{A}'_x}$. The continuity, $\widetilde{(A3)}$, becomes

$$\frac{\partial}{\partial x}(\tilde{u}D) + \frac{\partial}{\partial y}(\tilde{v}D) + \frac{\partial \omega}{\partial \sigma} = 0.$$

The baroclinic energy equation obtained by evaluating

$$D\tilde{u}\widetilde{(A1)} + D\tilde{v}\widetilde{(A2)} + \frac{\tilde{p}}{\rho_0}\widetilde{(A3)} + Dg\frac{\rho}{\rho_0}\left(-\frac{d\hat{\rho}}{dz}\right)^{-1} \tag{A4}$$

must then be vertically integrated to give (5).

The Princeton Ocean Model uses a staggered (Arakawa C) grid in the horizontal, defines the across-sigma velocity and turbulence quantities on the σ levels, and defines the horizontal velocity and density on the midpoint of the σ levels (Blumberg and Mellor 1987; Mellor 2004). All the terms in (4) and (5) are evaluated on the horizontal and vertical midpoints of the grid cells.

REFERENCES

Alford, M. H., M. Gregg, and M. A. Merrifield, 2006: Structure, propagation, and mixing of energetic baroclinic tides in Mamala Bay, Oahu, Hawaii. *J. Phys. Oceanogr.,* **36,** 997–1018.

Aucan, J., and M. A. Merrifield, 2008: Boundary mixing associated with tidal and near-inertial internal waves. *J. Phys. Oceanogr.,* **38,** 1238–1252.

——, ——, D. S. Luther, and P. Flament, 2006: Tidal mixing events on the deep flanks of Kaena Ridge, Hawaii. *J. Phys. Oceanogr.,* **36,** 1202–1219.

Balmforth, N. J., G. R. Ierley, and W. R. Young, 2002: Tidal conversion by subcritical topography. *J. Phys. Oceanogr.,* **32,** 2900–2914.

Blumberg, A. F., and G. L. Mellor, 1987: A description of a three-dimensional coastal ocean circulation model. *Three-Dimensional Coastal Ocean Models,* N. S. Heaps, Ed., Vol. 4, *Coastal and Estuarine Sciences,* Amer. Geophys. Union, 1–16.

Boyd, T. J., M. D. Levine, S. R. Gard, and W. Waldorf, 2005: Mooring observations from the Hawaiian Ridge. College of Oceanic and Atmospheric Sciences Rep. 2005-1, Oregon State University, 232 pp.

Carter, G. S., and M. C. Gregg, 2002: Intense, variable mixing near the head of Monterey Submarine Canyon. *J. Phys. Oceanogr.,* **32,** 3145–3165.

——, and ——, 2006: Persistent near-diurnal internal waves observed above a site of M_2 barotropic-to-baroclinic conversion. *J. Phys. Oceanogr.,* **36,** 1136–1147.

——, and M. A. Merrifield, 2007: Open boundary conditions for regional tidal simulations. *Ocean Modell.,* **18,** 194–209.

——, M. C. Gregg, and M. A. Merrifield, 2006: Flow and mixing around a small seamount on Kaena Ridge, Hawaii. *J. Phys. Oceanogr.,* **36,** 1036–1052.

Chavanne, C., 2007: Observations of the impact of mesoscale currents on internal tide propagation. Ph.D. thesis, University of Hawai'i and Manoa, 198 pp.

Chiswell, S. M., 1994: Vertical structure of the baroclinic tides in the central North Pacific subtropical gyre. *J. Phys. Oceanogr.,* **24,** 2032–2039.

Cummins, P. F., and L.-Y. Oey, 1997: Simulation of barotropic and baroclinic tides off northern British Columbia. *J. Phys. Oceanogr.,* **27,** 762–781.

Di Lorenzo, E., W. R. Young, and S. Llewellyn Smith, 2006: Numerical and analytical estimates of M_2 tidal conversion at steep oceanic ridges. *J. Phys. Oceanogr.,* **36,** 1072–1084.

Dushaw, B. D., B. M. Howe, B. D. Cornuelle, P. F. Worcester, and D. S. Luther, 1995: Barotropic and baroclinic tides in the central North Pacific Ocean determined from long-range reciprocal acoustic transmissions. *J. Phys. Oceanogr.,* **25,** 631–647.

Egbert, G. D., 1997: Tidal data inversion: Interpolation and inference. *Prog. Oceanogr.,* **40,** 53–80.

——, and R. D. Ray, 2000: Significant dissipation of tidal energy in the deep ocean inferred from satellite altimeter data. *Nature,* **405,** 775–778.

——, and ——, 2001: Estimates of M_2 tidal energy dissipation from TOPEX/Poseidon altimeter data. *J. Geophys. Res.,* **106,** 22 475–22 502.

——, and S. Y. Erofeeva, 2002: Efficient inverse modeling of barotropic ocean tides. *J. Atmos. Oceanic Technol.,* **19,** 183–204.

Eich, M. L., M. A. Merrifield, and M. Alford, 2004: Structure and variability of semidiurnal internal tides in Mamala Bay, Hawaii. *J. Geophys. Res.,* **109,** C05010, doi:10.1029/2003JC002049.

Flather, R. A., 1976: A tidal model of the north-west European continental shelf. *Mem. Soc. Roy. Sci. Liege,* **6,** 141–164.

Garrett, C., and E. Kunze, 2007: Internal tide generation in the deep ocean. *Annu. Rev. Fluid Mech.,* **39,** 57–87.

Gregg, M. C., 1987: Diapycnal mixing in the thermocline: A review. *J. Geophys. Res.,* **92,** 5249–5286.

Hodges, B. R., B. Laval, and B. M. Wadzuk, 2006: Numerical error assessment and a temporal horizon for internal waves in a hydrostatic model. *Ocean Modell.,* **13,** 44–46.

Holloway, P. E., and M. A. Merrifield, 1999: Internal tide generation by seamounts, ridges, and islands. *J. Geophys. Res.,* **104,** 25 937–25 951.

——, E. Pelinovsky, and T. Talipova, 1999: Modeling internal tide generation and evolution into internal solitary waves on the Australian North West Shelf. *Dynamics of Oceanic Internal Gravity Waves II: Proc. 'Aha Huliko'a Hawaiian Winter Workshop,* Honolulu, HI, University of Hawaii at Manoa, 43–49.

Johnston, T. M. S., and M. A. Merrifield, 2003: Internal tide scattering at seamounts, ridges, and islands. *J. Geophys. Res.,* **108,** 3180, doi:10.1029/2002JC001528.

——, ——, and P. E. Holloway, 2003: Internal tide scattering at the Line Islands Ridge. *J. Geophys. Res.,* **108,** 3365, doi:10.1029/2003JC001844.

Kang, S. K., M. G. G. Foreman, W. R. Crawford, and J. Y. Cherniawsky, 2000: Numerical modeling of internal tide generation along the Hawaiian Ridge. *J. Phys. Oceanogr.,* **30,** 1083–1098.

Katsumata, K., 2006: Tidal stirring and mixing on the Australian North West shelf. *Mar. Freshwater Res.,* **57,** 243–254.

Klymak, J. M., and Coauthors, 2006: An estimate of energy lost to turbulence at the Hawaiian Ridge. *J. Phys. Oceanogr.,* **36,** 1148–1164.

Kunze, E., L. K. Rosenfeld, G. S. Carter, and M. C. Gregg, 2002: Internal waves in Monterey Submarine Canyon. *J. Phys. Oceanogr.,* **32,** 1890–1913.

Lamb, K. G., 2004: Nonlinear interaction among internal wave beams generated by tidal flow over supercritical topography. *Geophys. Res. Lett.,* **31,** L09313, doi:10.1029/2003GL019393.

Larson, J. C., 1977: Cotidal charts for the Pacific Ocean near Hawaii using *f*-plane solutions. *J. Phys. Oceanogr.,* **7,** 100–109.

Lee, C. M., E. Kunze, T. B. Sanford, J. D. Nash, M. A. Merrifield, and P. E. Holloway, 2006: Internal tides and turbulence along the 3000-m isobath of the Hawaiian Ridge. *J. Phys. Oceanogr.,* **36,** 1165–1183.

Mahadevan, A., 2006: Modeling vertical motion at ocean fronts: Are nonhydrostatic effects relevant at submesoscales? *Ocean Modell.,* **14,** 222–240.

Martini, K. I., M. H. Alford, J. Nash, E. Kunze, and M. A. Merrifield, 2007: Diagnosing a standing wave in Mamala Bay, Oahu. *Geophys. Res. Lett.,* **34,** L17604, doi:10.1029/2007GL029749.

Mellor, G. L., 2004: User's guide for a three-dimensional, primitive equation, numerical ocean model. Program in Atmospheric and Oceanic Sciences Rep., Princeton University, 56 pp.

——, and T. Yamada, 1982: Development of a turbulence closure model for geophysical fluid problems. *Rev. Geophys. Space Phys.,* **20,** 851–875.

——, T. Ezer, and L.-Y. Oey, 1994: The pressure gradient conundrum of sigma coordinate ocean models. *J. Atmos. Oceanic Technol.,* **11,** 1126–1134.

Merrifield, M. A., and P. E. Holloway, 2002: Model estimates of M_2 internal tide energetics at the Hawaiian Ridge. *J. Geophys. Res.,* **107,** 3179, doi:10.1029/2001JC000996.

——, ——, and T. M. S. Johnston, 2001: The generation of internal tides at the Hawaiian Ridge. *Geophys. Res. Lett.,* **28,** 559–562.

Nash, J. D., E. Kunze, C. M. Lee, and T. B. Sanford, 2006: Structure of the baroclinic tide generated at Kaena Ridge, Hawaii. *J. Phys. Oceanogr.,* **36,** 1123–1135.

Niwa, Y., and T. Hibiya, 2001: Numerical study of the spatial distribution of the M_2 internal tide in the Pacific Ocean. *J. Geophys. Res.,* **106,** 22 441–22 449.

Oakey, N. S., 1982: Determination of the rate of dissipation of turbulent energy from simultaneous temperature and velocity shear microstructure measurements. *J. Phys. Oceanogr.,* **12,** 256–271.

Osborn, T. R., 1980: Estimates of the local rate of vertical diffusion from dissipation measurements. *J. Phys. Oceanogr.,* **10,** 83–89.

——, and W. R. Crawford, 1980: An airfoil probe for measuring

turbulent velocity fluctuations in water. *Air–Sea Interaction: Instruments and Methods,* F. Dobson, L. Hasse, and R. Davis, Eds., Plenum Press, 369–386.

Pinkel, R., and D. Rudnick, 2006: Editorial. *J. Phys. Oceanogr.,* **36,** 965–966.

Rattray, M., J. G. Dworski, and P. E. Kovala, 1969: Generation of long internal waves at the continental slope. *Deep-Sea Res.,* **16** (Suppl.), 179–195.

Ray, R. D., and G. T. Mitchum, 1996: Surface manifestation of internal tides generated near Hawaii. *Geophys. Res. Lett.,* **23,** 2101–2104.

——, and ——, 1997: Surface manifestation of internal tides in the deep ocean: Observations from altimetry and island gauges. *Prog. Oceanogr.,* **40,** 135–162.

Rudnick, D. L., and Coauthors, 2003: From tides to mixing along the Hawaiian Ridge. *Science,* **301,** 355–357.

Simmons, H. L., R. W. Hallberg, and B. K. Arbic, 2004: Internal wave generation in a global baroclinic tide model. *Deep-Sea Res. II,* **51,** 3043–3068.

Smith, W. H. F., and D. T. Sandwell, 1997: Global seafloor topography from satellite altimetry and ship depth soundings. *Science,* **277,** 1956–1962.

St. Laurent, L., and C. Garrett, 2002: The role of internal tides in mixing the deep ocean. *J. Phys. Oceanogr.,* **32,** 2882–2899.

Venayagamoorthy, S. K., and O. B. Fringer, 2005: Nonhydrostatic and nonlinear contributions to the energy flux budget in nonlinear internal waves. *Geophys. Res. Lett.,* **32,** L15603, doi:10.1029/2005GL023432.

Warner, J. C., C. R. Sherwood, H. G. Arango, and R. P. Signell, 2005: Performance of four turbulence closure models implemented using a generic length scale method. *Ocean Modell.,* **8,** 81–113.

Wesson, J. C., and M. C. Gregg, 1994: Mixing at Camarinal Sill in the Strait of Gibraltar. *J. Geophys. Res.,* **99,** 9847–9878.

Zaron, E. D., and G. D. Egbert, 2006a: Estimating open-ocean barotropic tidal dissipation: The Hawaiian Ridge. *J. Phys. Oceanogr.,* **36,** 1019–1035.

——, and ——, 2006b: Verification studies for a z-coordinate primitive-equation model: Tidal conversion at a mid-ocean ridge. *Ocean Modell.,* **14,** 257–278.